Effect of powder characteristics on production of oxide dispersion strengthened Fe[sbnd]14Cr steel by laser powder bed fusion

E. Vasquez, P.-F. Giroux, F. Lomello, M. Nussbaum, H. Maskrot, F. Schuster, P. Castany

Effect of powder characteristics on production of Oxide Dispersion Strengthened Fe-14Cr Steel by laser powder bed fusion

Authors

Elodie Vasquez[a], Pierre-François Giroux[a], Fernando Lomello[b], Matthieu Nussbaum[b], Hicham Maskrot[b], Frédéric Schuster[c], Philippe Castany[d]

[a] DEN-Service de Recherches Métallurgiques Appliquées, CEA, Université Paris-Saclay, F-91191, Gif-sur-Yvette, France

[b] DEN-Service d'Etudes Analytiques et de Réactivité des Surfaces, CEA, Université Paris-Saclay, F-91191, Gif-sur-Yvette, France

[c] CEA Cross-Cutting Program on Materials and Processes Skills, 91191 Gif-sur-Yvette, France

[d] Univ Rennes, INSA Rennes, CNRS, ISCR – UMR 6226, F-35000 Rennes, France

Corresponding author

Elodie Vasquez, +33 1 69 08 04 19, elodie.vasquez@cea.fr

Keywords

Additive manufacturing, Laser Powder Bed Fusion (L-PBF), Metal Matrix Composites (MMCs), Particle size distribution, Powder flowability, Chemical composition

1. Introduction

Oxide dispersion strengthened (ODS) ferritic steels are produced by powder metallurgical process. Mechanical alloying (MA) consists of milling Fe-14Cr stainless steel powder with Y_2O_3 and TiH_2 powders to distribute homogenously Ti and Y atoms inside the ferritic matrix. The resulting powder is then consolidated by hot extrusion or hot isostatic pressing to obtain a bulk material. This step allows the precipitation of Y-Ti-O oxides in the matrix, which lead to an improvement in mechanical and physical properties, especially for high temperature applications [1]. Considering the limitations regarding the final shape complexity of components obtained by these traditional fabrication routes, the evaluation and development of alternative production methods are currently studied in order to increase the widespread use of ODS alloys.

In the frame of assessing the potentialities of additive manufacturing to manufacture ODS complex parts, a Fe-14Cr powder milled with 0.3%wt. Y_2O_3 and 0.3%wt. TiH_2 is consolidated by Laser Powder Bed Fusion (L-PBF). This process depends on a wide range of parameters such as laser power, scanning speed, hatch distance, scanning strategy… An optimization of these parameters was performed to get dense L-PBF builds in a previous work [2]. The quality of L-PBF fabricated parts depends also on the powder feedstock characteristics.

Few works studied the influence of particle size distribution on the density of L-PBF builds. Spierings et al. compared the processability of three powders of 316L stainless steel (SS) with various particle size distributions by laser powder bed fusion [3]. They demonstrate that fine particles are

beneficial to get dense L-PBF parts and a better surface quality. Liu et al. showed that powder of 316L SS with high content of fines particles provides higher powder bed density and thus higher density parts under low laser energy intensity [4].

The influence of particle morphology on final properties of parts is not widely studied. Some researchers as Li et al. compared gas and water atomized powder [5]. They found that gas atomized spherical 316L powder generates parts with higher densities than those build with water atomized irregular powder. This is due to the high packing density and low oxygen content in gas-atomized powder. Baitimerov et al. compared three different batches of gas-atomized AlSi12 powder from different manufacturers [6]. They showed that the morphology of the powder affects the flowability and the apparent density. Powder with good flowability and apparent density combination show the best L-PBF processability. Spherical particles with a just amount of fine particles are necessary to get a uniform powder bed.

Further investigations on the influence of the powder characteristics on the properties of L-PBF builds is still necessary. Non-spherical ODS Fe-14Cr particles of milled powder and standard spherical atomized Fe-14Cr particles of powder are characterized for comparison. Observations and measurements such as density, particles size distribution, flowability and morphology are performed on these powders before consolidation by L-PBF process. This work aims to better understand the role of the powder's morphology on the L-PBF processability.

2. Materials and Methods

2.1. Materials

A Fe-14Cr-1W-0.3Mn-0.3Si-0.2Ni stainless steel powder, supplied by Nanoval, is used as matrix material. This gas atomized powder is labelled "Powder A" when used as-received and "Powder A30" when only the finest particles with a diameter lower than 30 µm are kept after sieving.

The powder A is milled with 0.3% wt. of Y_2O_3 oxide powder and 0.3% wt. of TiH_2 hydride powder. The milling is continuous and lasts for 176 hours. It was performed under hydrogen atmosphere with 100C6 balls by Mecachrome on MATPERF Platform. The milling process allows to distribute homogeneously the reinforcement in the metallic matrix. The integration of Y_2O_3 and TiH_2 aims at the formation of stable oxide particles such as $Y_2Ti_2O_7$ or Y_2TiO_5 in the stainless steel matrix [7,8]. The milled powder is labelled "Powder M" when used as-milled and "Powder M63" when this powder is sieved at 63 µm.

2.2. Selective laser melting

The L-PBF experiments are conducted on a TruPrint series 1000 L-PBF machine (TRUMPF GmbH), equipped with a 200 W Yb-fiber laser (λ=1.064 µm) and a spot size of 55 µm. The consolidation process is performed under argon atmosphere with an imposed oxygen concentration lower than 100 ppm during the process. The powder bed feed rate is fixed to 50 µm per layer. Parallel lines using bidirectional vectors are used as scanning direction. All samples consolidated by L-PBF process are cubes of 10 mm side.

In L-PBF, the processing parameters are usually combined in a volumetric energy density (E) defined by equation (1):

$$E = \frac{P}{V \times HD \times t} \quad (1)$$

where P is the laser power (W), V is the scan speed (mm.s^{-1}), HD is the hatch distance (mm) and t is layer thickness (mm) [9].

2.3. Analytical techniques

The theoretical densities are measured thanks to a helium pycnometer. The measurement of apparent density and flowability is performed using the Hall flowmeter funnel according to the ASTM B212 [10]. Tapped density is quantified with a Densitap ETD-20 from Granuloshop®, which follows the USP standard. Particles size distributions are determined thanks to a granulometer Partica LA-950 from Horiba®. The morphology of the powder is examined using a JEOL 7000F scanning electron microscope (SEM). Oxygen content of each powder are measured thanks to the inert gas fusion method using a Horiba® EMGA 820 AC analyser.

The L-PBF builds are analyzed in the as-grown conditions. The density of each sample is measured thanks to Archimedes' method. The measures are repeated twice for each sample. Specimens are then prepared for optical and SEM observations. Cross-sectional samples are polished following the standard metallographic procedures with a final polishing step using a 40 nm colloidal silica suspension in order to reveal the microstructure. SEM images are obtained thanks to a JEOL 7000F field emission gun (FEG) machine operating at 15 kV in backscattered electron (BSE) mode.

3. Results and discussion

3.1. Powder's comparison

Powder's characterization refers to the size, shape and surface roughness of particles. All these characteristics have to be considered in additive manufacturing since they play a significant role in flowability and packing efficiency. In this section, the most commonly powder characterization techniques are used in order to highlight the powder's characteristics, which affect preferentially the L-PBF processability.

Figure 1 shows SEM images of the four powder batches used in this study. Observations show that the atomized powders A and A30 are composed by spherical particles, contrary to the milled powders M and M63. Powder M presents some large particles, which are removed by sieving. Sieving to 63 µm allows to get more uniform sizes of particles and to decrease the median particle size (d_{50}) of about 12 µm, as shown in table 1. The four powder batches do not show oxides on the surface of the particles.

The particle size distributions, tapped densities and apparent densities of the four different powder batches evaluated in this study are presented in table 1. Powders M and M63 have respectively apparent densities of 3.7 and 3.6 g.cm^{-3}. No significant difference is observed between as-milled powder and sieved milled powder. The presence of large particles for powder M has no influence on the compactness of the powder.

Powder A30 contains only small particles with a diameter lower than 30 µm. In spite of the narrow size distribution of Powder A30, the tapped and apparent densities are relatively high. These

both parameters are not influenced by the smaller size distribution of powder particles contrary to the observations of McGeary and Karapatis [11,12]. They show that sphere diameters with various diameter ratios and volume compositions allows to better pack when compared with single-sized spheres (95.1% vs. 62.5% of the theoretical density respectively) [11]. Karapatis et al. show that it is necessary to have powder with suitable size ratio to improve the density of powder layer. Indeed, fine particles can fill voids left between coarse particles [12]. Powder A30 is composed by enough fine particles not to alter the packing efficiency in spite of a narrow size distribution.

The particles of powder A are finer than the particles of powder M. This difference in shape and size explains the difference in tapped and apparent densities in comparison with Powder M. Tapped density of powders M63 is lower than the one of powder M, due to their narrower size distributions.

Powder A and A30 present respectively apparent densities of 4.3 and 4.2 $g.cm^{-3}$. No significant difference is observed between these powders. Milled powder (M and M63) have apparent densities inferior to those of atomised powders (A and A30). This result can be explained by the non-spherical morphology of powder particles and by the lack of fine powder particles (inferior to 40 µm) for milled powders. Voids are left between coarse particles since no fine particles are present to fill the voids [12,13].

Powders M and M63 have respectively tapped densities of 4.7 and 4.4 $g.cm^{-3}$. The tapped densities are superior to the apparent densities. The non-spherical morphology of powder particles does not inhibit the rearrangement of powder particles. Tapped density of powder M63 is lower than the one of powder M, due to its narrower size distributions [11].

Powders A and A30 present respectively tapped densities of 4.9 and 5.1 $g.cm^{-3}$. These densities are superior to those of milled powders (M and M63). Figure 2 displays the particle size distributions in terms of volume fractions for the four different powder batches. It shows that powder A has a larger amount of fine particles (inferior to 40 µm) than milled powders. Sieving milled powder allows to reduce the presence of large particles. However, sieving does not compensate the lack of fine particles after milling, which alters the packing efficiency of milled powders.

Powders A and M63 have similar size distribution median particle size. Although the powder M63 has narrow particle size distribution, this characteristic enables the assessment of the effect of particle morphology on the L-PBF processability independently of the effect of size.

3.2. Estimation of apparent powder bed densities

A scraper spreads the powder during the L-PBF process. The powder bed apparent density is a compromise between tapped and apparent density, due to the effect of the scraper on the powder. Experiments were realised to estimate this powder bed apparent density. The powder is delivered uniformly on the substrate but only the borders of a cube with known internal dimensions is melted. After the build, the powder inside the cube is weighted and the apparent density of the powder bed can be determined, as presented in table 1.

Powders M and M63 have respectively powder bed apparent densities of 4 and 3.8 $g.cm^{-3}$ whereas powders A and A30 present respectively powder bed apparent densities of 4.5 and 4.2

g.cm^{-3}. The four powder bed apparent densities are comprised between the apparent and the tapped densities of the powders. These results show that the scraper packs the powder but not enough to compensate the difference in natural packing between spherical and non-spherical powders. Spherical powders allow to have powder layers with best densities than those obtained with no spherical powders. Best densities can be expected for L-PBF parts built with powders A and A30. since these powders have better apparent density than milled powders.

Powder A30 is the only powder to have an apparent density identical to the powder bed apparent density that means this powder is the only one not to pack by the scraper. Where the finest particles are put into motion by the scraper, they are probably subject to particles interactions. The powder particles inferior to 10 µm are indeed the most affected by attractive forces such as Van Der Waals forces and by agglomeration issues [13].

The d_{90} of powder A30 (26 µm) is inferior to the powder layer thickness (50 µm), which also explains why the scraper does not pack the powder A30. This difference in size allows the spreading of all the powder particles of powder A30 on the substrate in spite of particles interactions. This phenomenon explains why the powder bed apparent density of powder A30 is still superior to the powder bed apparent densities for milled powders (even if the milled powders are slightly packed by the scraper).

3.3. Comparison of flowability

For L-PBF applications, it is necessary to know how the powder flows when it is spread on the substrate. Several factors impact the powder flowability such as particle size, shape, cohesive and frictional interactions, humidity [14]... Table 2 regroups all the data on the flowability performance of each powder. Engeli et al. compare the processability of different Inconel 738LC powder batches and use, in particular, the span value to compare the flowability of their different powder batches.

The span value (S) is defined by equation (2):

$$S = \frac{(d_{90} - d_{10})}{d_{50}} \quad (2)$$

The span value measures the width of the size distribution of a powder. The smaller the value the narrower the distribution [15]. Powder A presents large size distributions, which explain the better arrangement observed for its particles contrary to those of milled powders (better apparent and tapped densities).

Sutton et al. present in their study other methods, as the Hausner ratio calculation and Hall flow test is an indicator to measure the powder flowability [16]. The Hausner ratio is linked to the flowability. This parameter is defined as the ratio between tapped and apparent densities. Abdullah et al. reports that powders with Hausner ratio inferior to 1.25 are considered as powders with good flowability and powders with Hausner ratio superior to 1.4 are considered as cohesive powders [17].

Powders A, A30, M and M63 present respectively Hausner ratio of 1.14; 1.21; 1.27 and 1.22. Only powder M has a Hausner ratio superior to 1.25, although is very close to 1.25. And all these powders can be spread on the substrate. Only powder M does not meet this requirement, since its Hausner ratio is though very close to 1.25.

The Hausner ratio of powder A30 is higher than the Hausner ratio of powder A (1.21 vs. 1.14). This phenomenon is attributed to a higher interparticle interactions for powder A30 since this powder presents a large amount of fine particles [18].

The Hall flow test is a measure of the amount of time for 50 g of powder to flow through the Hall flowmeter orifice (2.54 mm in diameter) [19]. Powders M and M63 present respectively Hall flows of 21 and 18 s/50g. Powder M63 flows quickly than powder M through the Hall flowmeter orifice. This result is probably linked to the presence of a small amount of particles with a size superior to 100 µm for powder M63, as showed in figure 2. These large particles could partially block the orifice and increase the Hall flow.

Powder A has a Hall flow of 18 s/50g, which is identical to the one of powder M63. These powders present the same median particle diameter but powder M63 has a narrower particle size distribution. Powder with a narrow particles size distribution usually flows better than powder with large particle size distribution [20].

Powders A and M63 present the same Hall flow, probably due to their similar size distributions.

Powder A30 does not flow naturally through the Hall flowmeter funnel, probably due to interparticle interactions (attractive forces, agglomerations, frictions…), which could block the orifice. As the surface area of a powder increases, the frictional and cohesive interactions frictions increase, which leads to less efficient flowability of this powder. The gravitational force is often the driving force to put into motion the powder particles [21]. As the particle diameter decreases, the influence of weight decreases and others forces such as frictions, agglomerations, Van der Waals interactions should be considered. Finally, the presence of fine particles (inferior to 10 µm) does not encourage the flowability of a powder.

Another method to compare the flowability of different powders consists in measuring the avalanche angle made by 100 cm^3 of powder contained in a rotating and transparent drum. This method is used by Spierings et al. to compare the powder flowability of a set of 21 different Fe- and Ni-based powders [22]. Powders with good flowability are characterized by a low avalanche angle value [22].

Powders M and M63 have respectively avalanche angles of 36 and 49 °. According to this indicator, powder M flows better than powder M63. Powder M contains a large amount of coarse particles (superior to 100 µm) as showed in figure 2. These coarse particles are driven by their weights and encourage a low avalanche angle.

Powders A and A30 present respectively avalanche angles of 33 and 41 °. The flowability of powder A is driven by its weight rather than the flowability of powder A30 is driven by other forces. Powder M63 has an avalanche angle 8 ° superior to the one of powder A30. The presence of large particle for powder M63 should encourage a lower avalanche angle that the one of powder A30. These results show that the morphology of powder particles also affects the flowability. There is mechanical interlocking between the non-spherical powder particles, which alters the flowability of powder M63. The morphology of powder particles play also a role on the flowability.

3.4. Influence of powder's characteristics on density of L-PBF builds

Consolidations by L-PBF process are performed with all the different powders following the same set of processing parameters. Figure 3 shows the evolution of the density of consolidated L-PBF samples as a function of energy density.

For energy densities superior to 100 J.mm^{-3}, the densities of parts built with the powders M and M63 are equal, as showed in figure 3. Removing the largest particles by sieving has a beneficial effect on the density of final parts only for 90 J.mm^{-3}. For this value of energy density, the finer the powder, the more dense the parts. Large particles require more energy to be completely melted and explain the decrease in density for parts made with powder M at 90 J.mm^{-3}.

The use of spherical powders (powders A and A30) leads to the increase in density of the final parts in comparison with non-spherical powders (powders M and M63) for energy densities inferior to 110 J.mm^{-3}. The finer the powder, the wider the processing range to obtain dense L-PBF parts. This phenomenon can be explained by the facility to melt fine powder particles. The better packing efficiencies of powders A and A30 measured previously increase the density of the powder bed and, in turn, their final parts' densities.

For energy densities superior to 110 J.mm^{-3}, no difference in terms of size and shape affects the densities of parts. A large kind of powders can be used in L-PBF process if the process parameters are choose in accordance with the powder's characteristics.

The densities of parts built with Powder M63 are higher than those built with Powder M for energy densities inferior to 180 J.mm^{-3} (Fig. 3). In the present study, powder M63 and powder A30 have narrow particles size distribution but generate parts with higher densities for the lowest value of energy densities in comparison with powder M and powder A respectively. Powder M contains probably not enough small particles to fill voids between coarse particles. It may be possible that powder M63 allows to get more homogeneous powder bed and consequently more homogeneous tracks during the laser melting, which improves the final part density.

Powder M presents higher tapped density than powder M63. However, powders M and M63 have similar apparent densities. Since powder M63 generates L-PBF parts with higher densities than those made with powder M, it can be concluded that the apparent density is the most relevant parameter to compare L-PBF processability of various powders.

3.5. Influence of powder's characteristics on microstructure of L-PBF builds

Two kinds of microstructures are obtained with the four powders after L-PBF consolidation, as seen on figure 4. Columnar grains oriented only along the building direction are obtained for the ODS Fe-14Cr samples (those made with powders M and M63). Materials made with powders A and A30 present a stirred microstructure composed by columnar grains, not necessary oriented along the building direction and by equiaxed grains. a stirred microstructure for the Fe-14Cr samples (those made with Powders A and A30) and columnar grains for the ODS Fe-14Cr samples (those made with Powders M and M63).

Powders A and M63 have similar mean particle diameters but the materials elaborated from these powders have different microstructures. The size of the powder does not have a significant impact on the final microstructure. The powder morphology might interfere on the laser-matter interaction.

In order to clarify this point for this study, the powder A was also milled without addition of reinforcements to give powder AM on figure 5a and b. This experiment allows to investigate both the effect of the morphology of the powder and the influence of the milling process on the L-PBF consolidation. Powder AM was sieved at 80 µm before consolidation to obtain a median particle diameter of 82.7 µm. This powder has the same chemical composition than powder A and the same morphology than powder M.

Figure 5c shows that L-PBF build made from powder AM has a stirred microstructure as materials processed with powders A and A30. Consequently, the morphology of the powder does not interferes significantly on the final microstructure.

Figure 6 shows SEM images on the samples' microstructure made with powders A, AM and M63, perpendicular to the building direction. On the Fe-14Cr samples, two kinds of grains are visible: small grains surrounded by large grains. grains are finer along the borders of tracks and larger inside the tracks. On the contrary, ODS Fe-14Cr sample presents grains with homogeneous size inside the tracks.

The grains growth differently between a Fe-14Cr and an ODS Fe-14Cr samples.

The presence of yttrium, titanium and oxygen, leading to the nucleation of Y-Ti-O mixed oxides in the ODS Fe-14Cr sample, influences significantly the microstructure of solidification. These oxides might act as stabilizers of the microstructure.

Finally, The last difference, which could explain these differences in terms of microstructure of solidification, between all these powders is their chemical composition. Powders M and M63 contain 0.3 wt. % yttrium and 0.3 wt. % titanium, contrary to the others powders A and A30. Table 3 compares the oxygen level in the different powders. Powder M63 has a higher oxygen content in comparison with the two other powders A and A30 (about 450 ppm). This result could be attributed to the addition of Y_2O_3 and/or contamination during the milling. These differences in terms of chemical composition could interfere the morphology of the melt pool and thus the grain's growth. This phenomenon is discussed in more details in part 4.3.

3.6. Influence of microstructure solidification on mechanical properties

Tensile tests are performed on materials elaborated from powder A (Fe-14Cr) and from powder M63 (ODS Fe-14Cr). Figure 7 presents the room temperature tensile curves of Fe-14Cr samples and of ODS Fe-14Cr.

The samples elaborated from powder A at 175 W; 100 $mm.s^{-1}$ and 195 µm showed ductile fractures whereas samples elaborated from powder M63 with the same processing parameters showed brittle fractures. Fe-14Cr samples present a yield strength of 520 MPa and an ultimate tensile strength of 553 MPa whereas the ODS Fe-14Cr samples have an ultimate tensile strength of 207 MPa. The presence of fine and dispersed uniformly inside the matrix Y-Ti-O particles, studied in a previous study [2], should increases the tensile properties, as showed in conventional ODS samples

(elaborated by extrusion) [23]. However, in this study, the effect of the nano-particles is diminished by the presence of micrometric inclusions rich in yttrium, titanium and oxygen revealed by fractographic analysis.

The ODS samples elaborated from powder M63 at 100 W; 50 mm.s^{-1} and 100 µm showed ductile fracture. These materials present a yield strength of 392 MPa and an ultimate tensile strength of 447 MPa. These properties are still inferior to those of Fe-14Cr samples. The transition between brittle and ductile fracture is linked to the decreases of the size of the inclusions observed on fractographic SEM images. The use of a low laser power (100 W) is probably the reason explaining the enhancement in tensile properties since high laser power encourages the formation of micrometric inclusions.

For the elaboration of ODS Fe-14Cr by L-PBF process, the choice of processing parameters has to be made as function of powder characteristics but also as a function of the precipitation of Y-Ti-O particles. The processing parameters should allow to obtain dense sample with the minimum (or none) micrometric inclusions. A decrease in reinforcement ratio could allow better mechanical properties.

4. Discussion

4.1. Selection of flowability indicator

Powder M has an avalanche angle very close to that one of powder A (36 and 33 °). The use of this unique flowability indicator would lead to the conclusion that powders M and A have Powder A and powder M present similar avalanche angle, that means these powders should have similar flowability. However, it was found previously that powder A presents better apparent density, tapped density and apparent powder bed density Hausner ratio and span value than powder M and consequently better flowability. The avalanche angle cannot be used as unique flowability indicator.

Powders A30 and M63 present similar Hausner ratio (1.21 and 1.22). However, powder A30 allows to obtain powder layers with best densities than those obtained with powder M63. The use of this unique indicator to compare the performance of a powder during L-PBF process is not enough. This conclusion is in agreement with the works of Schulze and Spierings et al. [22,24].

Powder M63 has the same similar Hausner ratio than Powder A30 and similar Hall flow than Powder M (18 s/50g). Nonetheless, this powder has a higher avalanche angle value than this powder these both powders. All these data show that the comparison of the powder flowability is complicated and cannot be related to only one parameter. It is still necessary to define specific requirements for powders used in L-PBF process, as also explain by Tan et al. [13]. These requirements have to depend on the size but also on the morphology of the powder particles. The interaction between the powder and the scraper has also to be considered. Clayton et al. explained that a powder can be adapted for one use but poor for another application [25]. The powder and the process have to match well. They agreed on the fact that only one parameter (Hausner ratio, Hall flowmeter…) cannot describe the powder flowability correctly.

The morphology of particles has a strong influence on the properties of the final material, confirming the results obtained by Spierings et al. [26]. The authors manufacture L-PBF samples employing standard Inconel 625 as well as ODS Inconel 625 powders. Their study shows that the processing parameters range is much narrow when ODS Inconel 625 powder is used due to its

irregular shape. The morphology of the particles does not only affect the flowability but also the laser / powder interactions. Attar et al. study also the effect of powder particle shape on final properties of Ti-TiB composite materials [27]. They obtain better density and mechanical properties with the most spherical powder particles.

Liu et al. showed that powders with different particles size distributions act differently in L-PBF process [4]. They found that powders with a wide range of distribution size give parts with high densities under low laser energy densities.

However, Scipioni Bertoli et al. compare the behaviour of a gas atomized powder and a water atomized powder of 316L [28]. The water-atomized powder is composed by irregularly-shaped particles whereas the gas atomized powder has spherical particles. Although this difference in shape, both powders have similar laser absorptivity and give similar track morphology and melt pool dynamics.

4.2. Role of chemical composition on the solidification microstructure

Previous results discussed before show that the chemical composition of the powder would be the main factor to explain the difference observed in solidification microstructure. Several authors observed also that the presence of alloying elements influences the melt pool shape.

Niu and Chang explained that a large thermal gradient is developed between the centre and edge of the melt pool since a laser beam follows a Gaussian distribution of energy [29]. As the surface tension is a function of temperature, the existence of this thermal gradient causes a variation of surface tension between the centre and edge of the melt pool, which induces Marangoni flow. They explained that For pure iron with low oxygen content, the surface tension decreases when the temperature increases rather than for iron with high oxygen content, the surface tension increases when the temperature increases [30]. Material convection in the melt pool depends on the magnitude of the gradient of surface tension to temperature, according to the Marangoni effect [31]. This phenomenon creates wide and shallow scan tracks for a low oxygen content and deep and narrow scan tracks for a high oxygen content.

Niu and Chang compared the behaviour of gas and water atomized high steel powders. The gas atomized powder contains 200 ppm of oxygen whereas the water atomized powders contain 1000 and 1700 ppm of oxygen. Thanks to its low oxygen level, the gas atomized powder allows the formation of wide and shallow scan tracks, since the Marangoni flow occurs from the centre to the edge of the melt pool. In the contrary, water atomised powders, with high oxygen level, lead to the formation of deep and narrow scan tracks, since the Marangoni flow occurs from the edge to the centre of the melt pool [29].

Simchi et al. observed also that the presence content of oxygen during the heating and the melting of iron powders in laser sintering process strongly influences the densification and the microstructure. The powder with high oxygen content (superior to 0.59 wt. %) leads to the formation of parts with numerous porosities oriented along the building direction. They attributed these porosities to the formation of deep and narrow scan tracks [32]. They concluded that an oxide layer on the surface of powder particles increases significantly the absorption of CO_2 laser radiation, as corroborated by

Tolochko et al. [33]. They observed also that the presence of oxide particles affects the solidification and refines the grain structure.

These both studies agree with the fact that the content of oxygen inside a powder influences the melt pool shape and consequently the grain growth. However the minimal amount of oxygen needed to change the convection's direction of Marangoni flow varies between these studies.

On the contrary, Kruth et al. reported that an increase in oxygen content leads to large molten pools due to exothermal reaction of iron oxidation [34].

On the contrary, Rombouts et al. found that a large amount of oxygen (3 wt. %) inside the consolidation chamber results in an enlargement of the scan tracks. The oxygen could dissolve in the liquid metal. The amount of oxygen incorporated inside the iron matrix could exceed the equilibrium oxygen concentration in liquid iron, which is 0.4 wt. % at 1700 °C. Upon cooling and at oxygen contents exceeding the maximal dissolved oxygen content, iron oxides are formed by exothermic reactions. The energy release near the melt pool by theses reactions contributes to the enlargement of the melt pool if enough energy are released [35].

It is necessary to differentiate the effect of oxygen, which could act as a surfactant and causes an inversion of the Marangoni flow and the presence of oxygen, which lead to oxides formation. A high amount of oxygen should produce narrow and deep scan tracks. However, if this oxygen are used to form oxides, the energy released by theses reactions produces wide and shallow scan tracks.

Rombouts et al. studied also the effect of various elements (Ti, Cu, O, Si, C) on the quality of L-PBF iron-based parts [35]. They concluded that the presence of deoxidizer elements such as titanium or silicon leads to a larger molten pool and a higher tendency to balling. The exothermic formation of oxides and carbides plays an important role on the instability of the molten pool. Similarly, Engeli et al. found that the silicon content has to be lower than 0.03 wt. % in order to obtain a low cracking susceptibility in Inconel 738LC [15].

Zhang et al. explained that yttrium has a strong deoxygenation capacity and form oxides quickly during L-PBF process [36]. In conventional welding, Haoyang et al. indicated that the surface tension of yttrium is lower than iron, and yttrium transferred into the weld pool decreases the surface tension of the molten metal [37]. They found that the optimum yttrium content is about 1.125 wt. %. All these studies revealed that alloying elements have a significant influence on the final microstructure of L-PBF parts.

In the present study, samples are characterized by high oxygen contents (from 1300 to 1800 ppm depending on their chemical composition). The difference between the measured values is not significant enough to conclude on a potential impact of oxygen content to explain the difference in microstructure observed between powders A, AM and M63.

Titanium and yttrium form oxides. Theses exothermic reactions enlarge the melt pool. In addition, the presence of yttrium encourages the formation of wide scan tracks by decreasing the surface tension of the liquid metal.

In the present study, titanium and yttrium are added in only a small proportion around 0.3 wt. %. But these elements act on the microstructure of solidification, even though in low amount, probably by having an impact on the molten pool flow. It is known that grains grow perpendicularly to the molten

pool boundary [38]. The results can be explained by the larger molten pool induced by the addition of yttrium and titanium, which leads to the growth of regular columnar grains along the building direction (fig. 8b). On the contrary, without the presence of titanium and yttrium, the molten pool is deeper and grains growth follows several directions, leading to a stirred microstructure (fig. 8a). This hypothesis is in accordance with the measured of the melt pools realised on ODS Fe-14Cr samples. The width of melt pool for ODS samples are measured around 300 µm and the depth are estimated between 60-70 µm. Additional characterizations of the molten pool would be performed in order to validate this hypothesis.

5. Conclusions

In this work, the influence of powder characteristics in terms of size, shape and chemistry is studied. The following conclusions can be drawn:

- Spherical powder particles allow to obtain L-PBF builds with higher densities than those made with non-spherical powder particles.
- Fine powder particles give a broader L-PBF processing parameter range for obtaining dense L-PBF parts.
- Non-spherical powder can be used in L-PBF process. For energies densities above 110 J.mm^{-3}, the influence of the shape and size on the density of L-PBF builds is significantly reduced.
- Only one flowability indicator cannot predict the behavior of a powder during L-PBF process.
- Chemical composition of the powder strongly influences the final microstructure of L-PBF parts. Yttrium and titanium induce the formation of large and shallow molten pools, which lead to the growth of regular columnar grains along the building direction.

Acknowledgements:

The authors would like to thanks both laboratories LTMEx and LISL from CEA with a specific thanks to E. Bouaravong, O. Hercher, J. Varlet and C. Sauder.

References

[1] A. Wasilkowska, M. Bartsch, U. Messerschmidt, R. Herzog, A. Czyrska-Filemonowicz, Creep mechanisms of ferritic oxide dispersion strengthened alloys, Journal of Materials Processing Technology. 133 (2003) 218–224. doi:https://doi.org/10.1016/S0924-0136(02)00237-6.

[2] E. Vasquez, P.-F. Giroux, F. Lomello, A. Chniouel, H. Maskrot, F. Schuster, P. Castany, Elaboration of oxide dispersion strengthened Fe-14Cr stainless steel by selective laser melting, Journal of Materials Processing Technology. 267 (2019) 403–413. doi:https://doi.org/10.1016/j.jmatprotec.2018.12.034.

[3] A. b. Spierings, N. Herres, G. Levy, Influence of the particle size distribution on surface quality and mechanical properties in AM steel parts, Rapid Prototyping Journal. 17 (2011) 195–202. doi:10.1108/13552541111124770.

[4] Liu, B., Wildman, R., Tuck, C., Ashcroft, I.,, Hague, R., Investigation the effect of particle size distribution on processing parameters optimization in selective laser melting process, in: Austin, Texax, USA, 2011: pp. 227–238.

[5] R. Li, Y. Shi, Z. Wang, L. Wang, J. Liu, W. Jiang, Densification behavior of gas and water atomized 316L stainless steel powder during selective laser melting, Applied Surface Science. 256 (2010) 4350–4356. doi:10.1016/j.apsusc.2010.02.030.

[6] R. Baitimerov, P. Lykov, D. Zherebtsov, L. Radionova, A. Shultc, K.G. Prashanth, Influence of Powder Characteristics on Processability of AlSi12 Alloy Fabricated by Selective Laser Melting, Materials (Basel). 11 (2018). doi:10.3390/ma11050742.
[7] S.-Y. Zhong, J. Ribis, N. Lochet, Y. de Carlan, V. Klosek, V. Ji, M.-H. Mathon, The Effect of Y/Ti Ratio on Oxide Precipitate Evolution in ODS Fe-14 Wt Pct Cr Alloys, Metallurgical and Materials Transactions A. 46 (2015) 1413–1418. doi:10.1007/s11661-014-2683-5.
[8] M.K. Miller, E.A. Kenik, K.F. Russell, L. Heatherly, D.T. Hoelzer, P.J. Maziasz, Atom probe tomography of nanoscale particles in ODS ferritic alloys, Materials Science and Engineering: A. 353 (2003) 140–145. doi:10.1016/S0921-5093(02)00680-9.
[9] H. Fayazfar, M. Salarian, A. Rogalsky, D. Sarker, P. Russo, V. Paserin, E. Toyserkani, A critical review of powder-based additive manufacturing of ferrous alloys: Process parameters, microstructure and mechanical properties, Materials & Design. 144 (2018) 98–128. doi:10.1016/j.matdes.2018.02.018.
[10] ASTM B212-17, Standard Test Method for Apparent Density of Free-Flowing Metal Powders Using the Hall Flowmeter Funnel, ASTM International, West Conshohocken, PA. (2017). doi:10.1520/b0212-17.
[11] McGeary, Mechanical Packing of Spherical Particles, Journal of the American Ceramic Society. 44 (1961) 513–522.
[12] N.P. Karapatis, G. Egger, P.E. Gygax, R. Glardon, Optimization of Powder Layer Density in Selective Laser Sintering, Solid Freeform Fabrication Proceedings. (1999) 255–263.
[13] J.H. Tan, W.L.E. Wong, K.W. Dalgarno, An overview of powder granulometry on feedstock and part performance in the selective laser melting process, Additive Manufacturing. 18 (2017) 228–255. doi:10.1016/j.addma.2017.10.011.
[14] W. Ding, G. Chen, M. Qin, Y. He, X. Qu, Low-cost Ti powders for additive manufacturing treated by fluidized bed, Powder Technology. 350 (2019) 117–122. doi:10.1016/j.powtec.2019.03.042.
[15] R. Engeli, T. Etter, S. Hövel, K. Wegener, Processability of different IN738LC powder batches by selective laser melting, Journal of Materials Processing Technology. 229 (2016) 484–491. doi:10.1016/j.jmatprotec.2015.09.046.
[16] A.T. Sutton, C.S. Kriewall, M.C. Leu, J.W. Newkirk, Powder characterisation techniques and effects of powder characteristics on part properties in powder-bed fusion processes, Virtual and Physical Prototyping. 12 (2017) 3–29. doi:10.1080/17452759.2016.1250605.
[17] E.C. Abdullah, D. Geldart, The use of bulk density measurements as flowability indicators, Powder Technology. 102 (1999) 151–165. doi:10.1016/S0032-5910(98)00208-3.
[18] A.B. Yu, J.S. Hall, Packing of fine powders subjected to tapping, Powder Technology. 78 (1994) 247–256. doi:10.1016/0032-5910(93)02790-H.
[19] ASTM B213-17, Standard Test Methods for Flow Rate of Metal Powders Using the Hall Flowmeter Funnel, ASTM International. (2017).
[20] S. Vock, B. Klöden, A. Kirchner, T. Weißgärber, B. Kieback, Powders for powder bed fusion: a review, Prog Addit Manuf. (2019). doi:10.1007/s40964-019-00078-6.
[21] C. Pleass, S. Jothi, Influence of powder characteristics and additive manufacturing process parameters on the microstructure and mechanical behaviour of Inconel 625 fabricated by Selective Laser Melting, Additive Manufacturing. 24 (2018) 419–431. doi:10.1016/j.addma.2018.09.023.
[22] A.B. Spierings, M. Voegtlin, T. Bauer, K. Wegener, Powder flowability characterisation methodology for powder-bed-based metal additive manufacturing, Prog Addit Manuf. 1 (2016) 9–20. doi:10.1007/s40964-015-0001-4.
[23] D.A. McClintock, M.A. Sokolov, D.T. Hoelzer, R.K. Nanstad, Mechanical properties of irradiated ODS-EUROFER and nanocluster strengthened 14YWT, Journal of Nuclear Materials. 392 (2009) 353–359.
[24] D. Schulze, ed., Flow properties of bulk solids, in: Powders and Bulk Solids: Behavior, Characterization, Storage and Flow, Springer Berlin Heidelberg, Berlin, Heidelberg, 2008: pp. 35–74. doi:10.1007/978-3-540-73768-1_3.
[25] J. Clayton, D. Millington-Smith, B. Armstrong, The Application of Powder Rheology in Additive Manufacturing, JOM. 67 (2015) 544–548. doi:10.1007/s11837-015-1293-z.
[26] Spierings, Bauer, T, Dawson, K, Colella, A, Wegener, K, Processing ODS Modified IN625 using Selective Laser Melting, SFF. (2015).
[27] H. Attar, K.G. Prashanth, L.-C. Zhang, M. Calin, I.V. Okulov, S. Scudino, C. Yang, J. Eckert, Effect of Powder Particle Shape on the Properties of In Situ Ti–TiB Composite Materials Produced by Selective Laser Melting, Journal of Materials Science & Technology. 31 (2015) 1001–1005. doi:10.1016/j.jmst.2015.08.007.

[28] U. Scipioni Bertoli, G. Guss, S. Wu, M.J. Matthews, J.M. Schoenung, In-situ characterization of laser-powder interaction and cooling rates through high-speed imaging of powder bed fusion additive manufacturing, Materials & Design. 135 (2017) 385–396. doi:10.1016/j.matdes.2017.09.044.
[29] H.J. Niu, I.T.H. Chang, Selective laser sintering of gas and water atomized high speed steel powders, Scripta Materialia. 41 (1999) 25–30. doi:10.1016/S1359-6462(99)00089-5.
[30] K.C. Mills, B.J. Keene, R.F. Brooks, A. Shirali, Marangoni effects in welding, Philosophical Transactions of the Royal Society of London. Series A: Mathematical, Physical and Engineering Sciences. 356 (1998) 911–925. doi:10.1098/rsta.1998.0196.
[31] T. Mukherjee, V. Manvatkar, A. De, T. DebRoy, Dimensionless numbers in additive manufacturing, Journal of Applied Physics. 121 (2017) 064904. doi:10.1063/1.4976006.
[32] A. Simchi, The role of particle size on the laser sintering of iron powder, Metall and Materi Trans B. 35 (2004) 937–948. doi:10.1007/s11663-004-0088-3.
[33] Tolochko, N., Mozzharov, S.E., Sobolenko, N.V., Khlopkov, Yu. V., Yadroitsev, I.A., Mikhailov, V.B., Main relationships governing laser sintering of loose single-component metallic powders, Journal of Advanced Materials. 2 (1995) 151–57.
[34] J.-P. Kruth, G. Levy, F. Klocke, T.H.C. Childs, Consolidation phenomena in laser and powder-bed based layered manufacturing, CIRP Annals - Manufacturing Technology. 56 (2007) 730–759. doi:10.1016/j.cirp.2007.10.004.
[35] M. Rombouts, J.P. Kruth, L. Froyen, P. Mercelis, Fundamentals of Selective Laser Melting of alloyed steel powders, CIRP Annals - Manufacturing Technology. 55 (2006) 187–192. doi:10.1016/S0007-8506(07)60395-3.
[36] Y. Zhang, J. Zhang, Q. Yan, L. Zhang, M. Wang, B. Song, Y. Shi, Amorphous alloy strengthened stainless steel manufactured by selective laser melting: Enhanced strength and improved corrosion resistance, Scripta Materialia. 148 (2018) 20–23. doi:10.1016/j.scriptamat.2018.01.016.
[37] D. Haoyang, S. Dongyun, H. Laichang, Y. Jian, Y. Yongmei, R. Zhen'an, Effect of Trace Yttrium Oxide on High and Low Temperature Properties of 9Cr-1Mo Weld Joint for Super Critical Unit, Rare Metal Materials and Engineering. 43 (2014) 2064–2068. doi:10.1016/S1875-5372(14)60149-1.
[38] T. DebRoy, H.L. Wei, J.S. Zuback, T. Mukherjee, J.W. Elmer, J.O. Milewski, A.M. Beese, A. Wilson-Heid, A. De, W. Zhang, Additive manufacturing of metallic components – Process, structure and properties, Progress in Materials Science. 92 (2018) 112–224. doi:10.1016/j.pmatsci.2017.10.001.

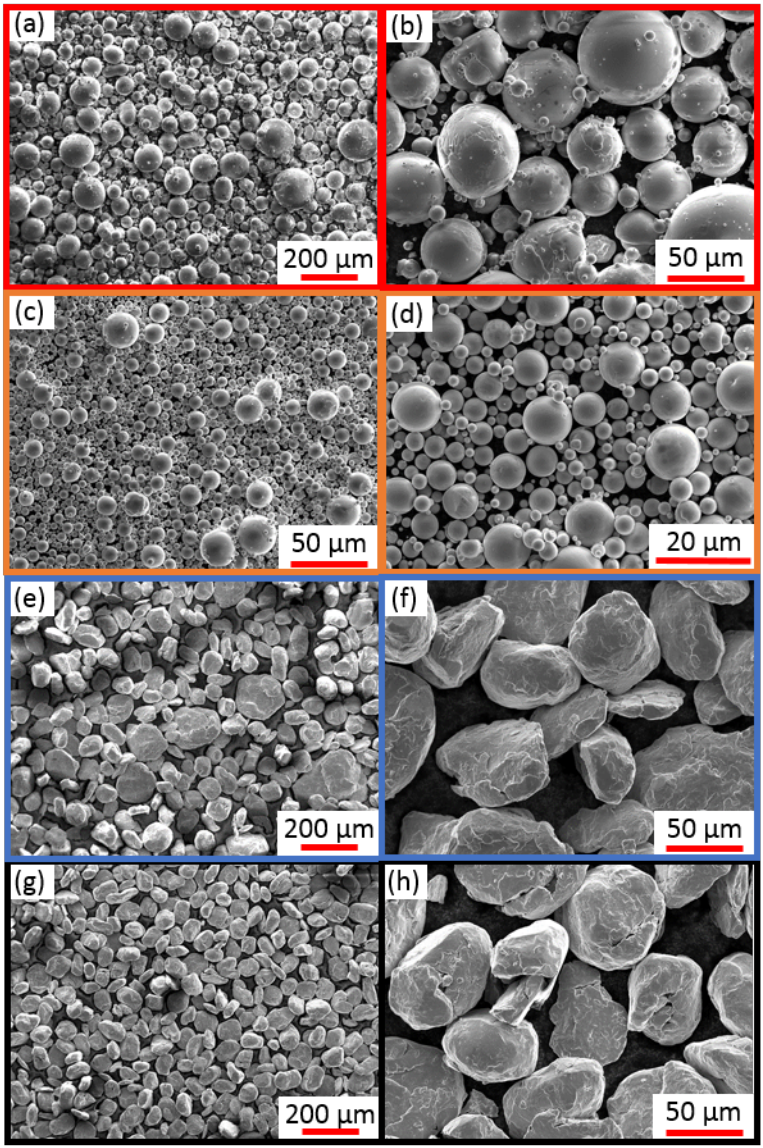
Powder A
(a)
200 µm
(b)
50 µm
Powder A30
(c)
50 µm
(d)
20 µm
Powder M
(e)
200 µm
(f)
50 µm
Powder M63
(g)
200 µm
(h)
50 µm

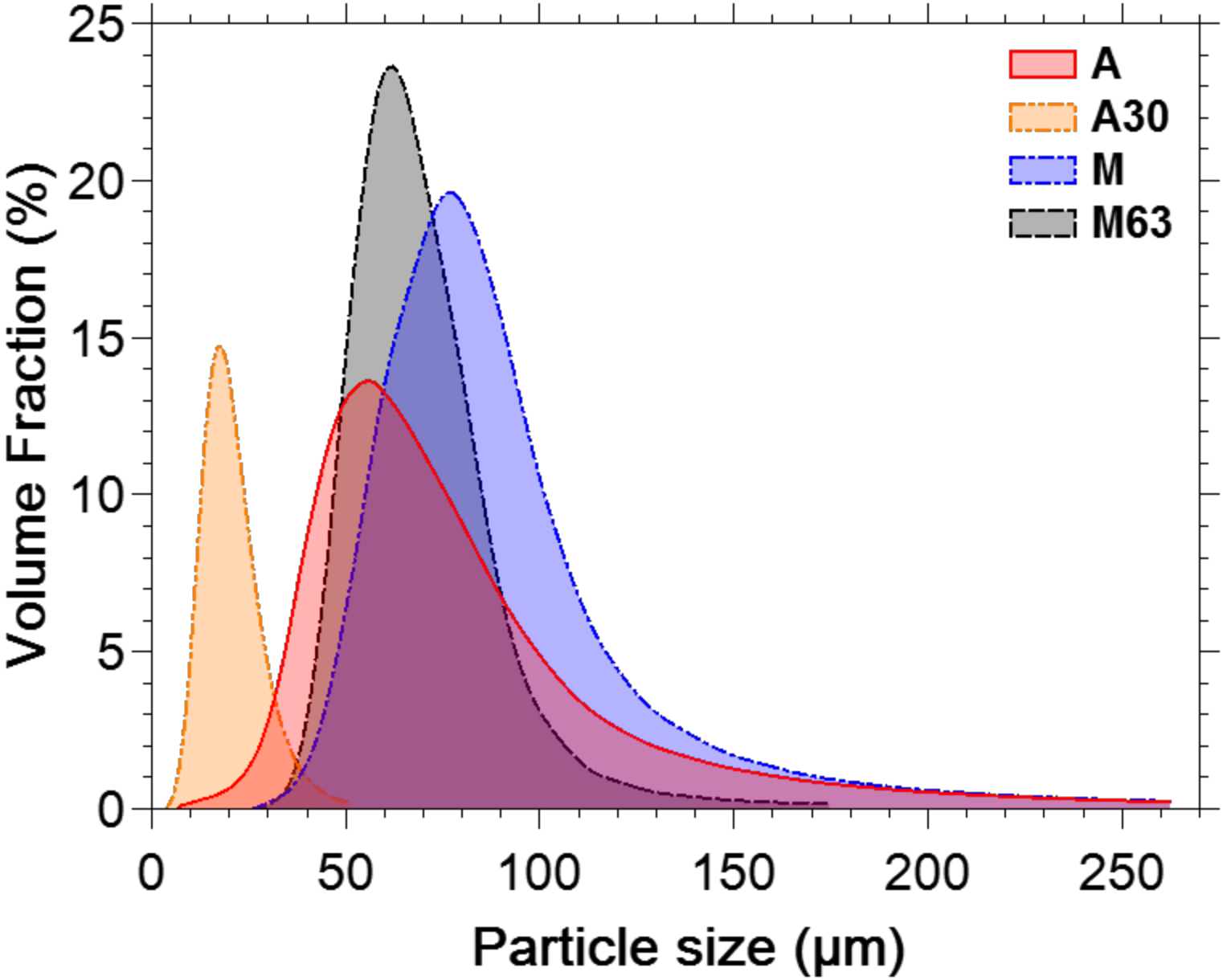
A
A30
M
M63
Volume Fraction (%)
0
5
10
15
20
25
0
50
100
150
200
250
Particle size (μm)

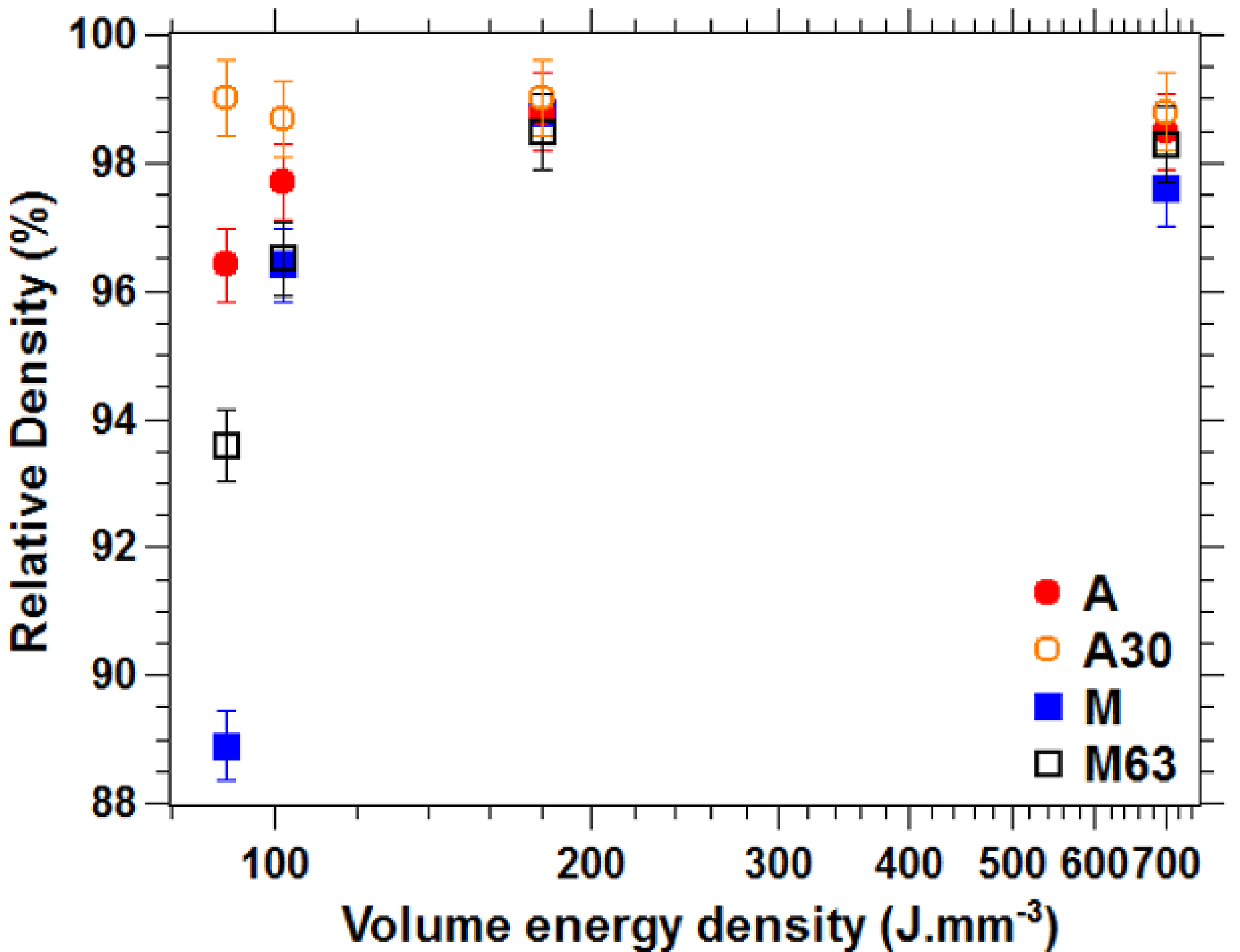
Relative Density (%)
100
98
96
94
92
90
88
100
200
300
400
500
600
700
Volume energy density (J.mm-3)
A
A30
M
M63

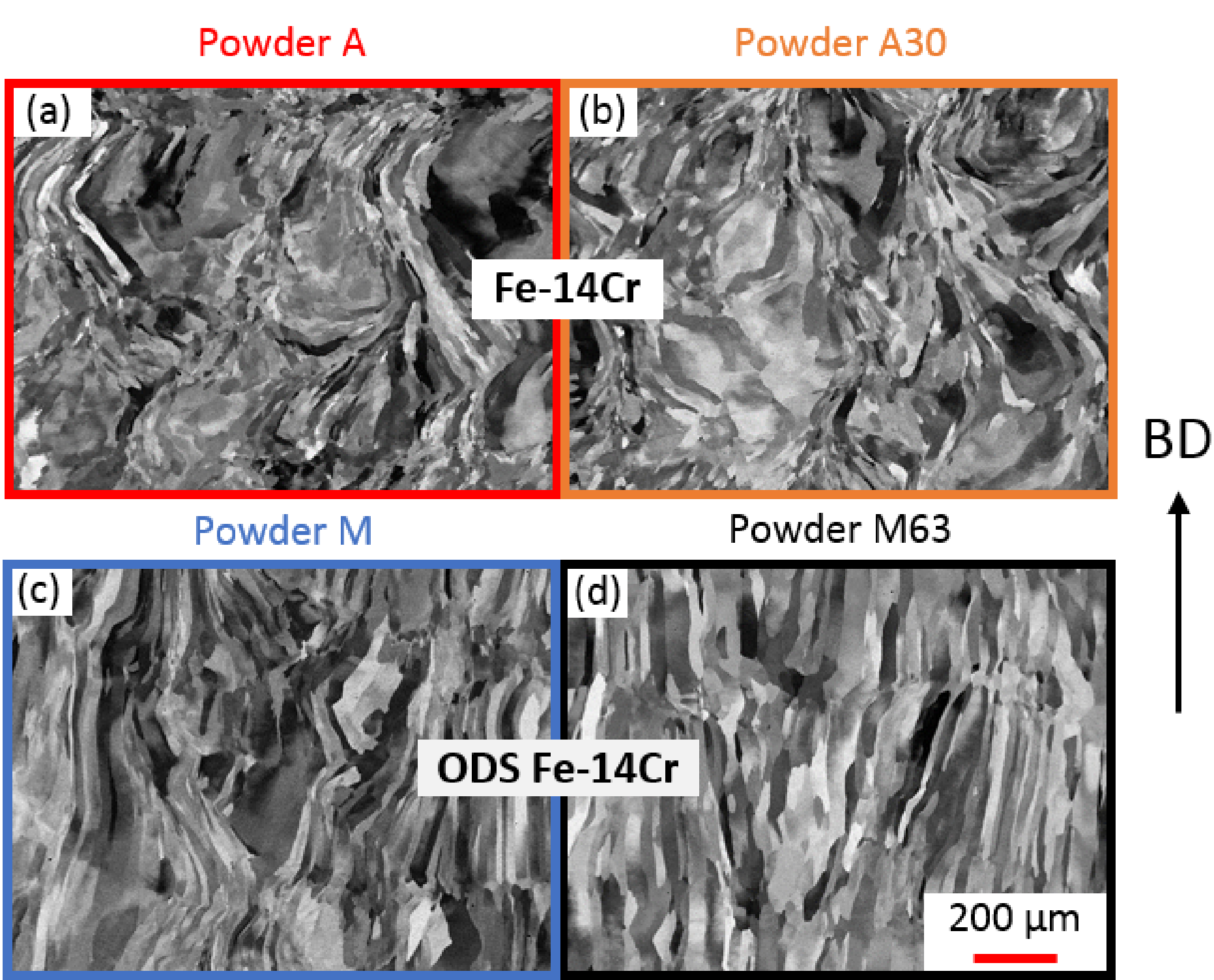
Powder A
Powder A30
(a)
(b)
Fe-14Cr
BD
Powder M
Powder M63
(c)
(d)
ODS Fe-14Cr
200 µm

Powder AM

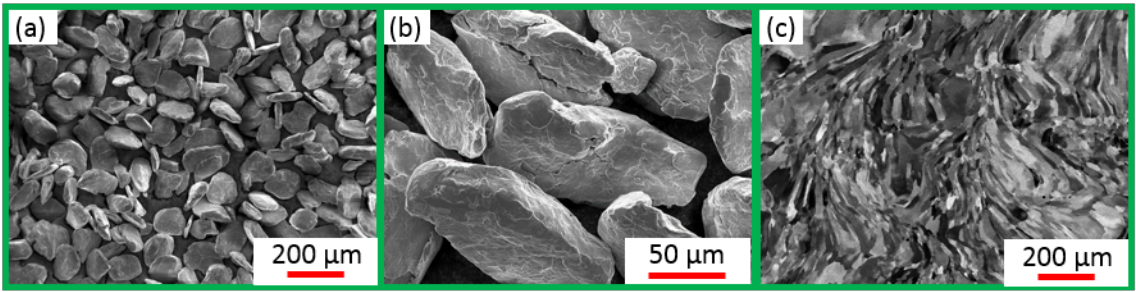

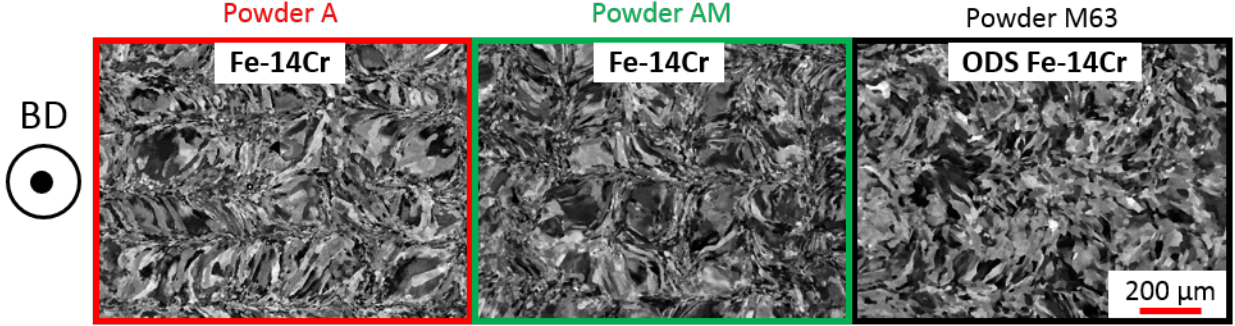
Powder A
Powder AM
Powder M63
BD
Fe-14Cr
Fe-14Cr
ODS Fe-14Cr
200 µm

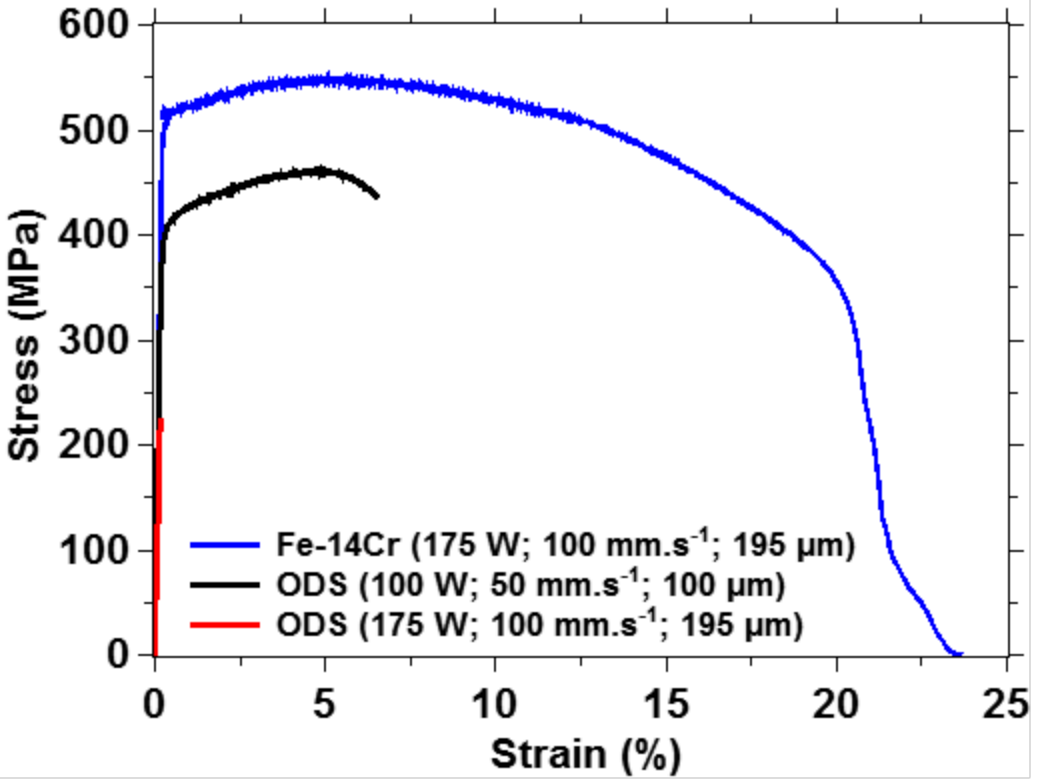
600
500
400
300
200
100
0
Stress (MPa)
0
5
10
15
20
25
Strain (%)
Fe-14Cr (175 W; 100 mm.s-1; 195 µm)
ODS (100 W; 50 mm.s-1; 100 µm)
ODS (175 W; 100 mm.s-1; 195 µm)

Fe-14Cr

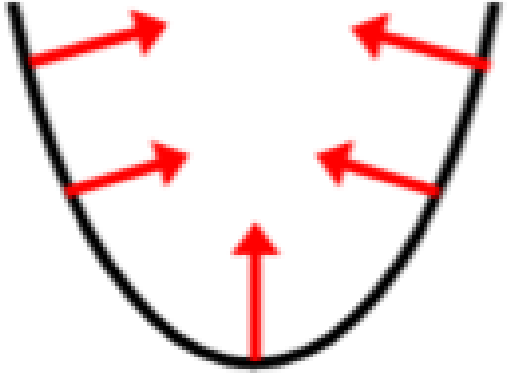

(a) High oxygen content

ODS Fe-14Cr

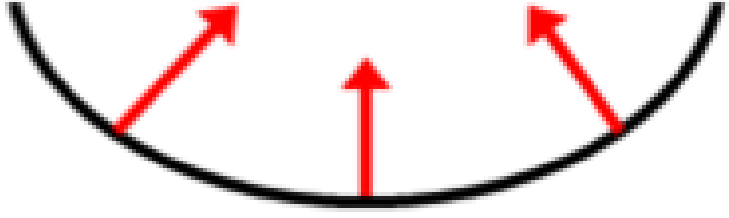

(b) High oxygen content with presence of yttrium and titanium

Table 1: Granulometric analysis and densities of powders A, A30, M and M63.

Powder	d_{10} (µm)	d_{50} (µm)	d_{90} (µm)	Density ($g.cm^{-3}$)	Tapped density ($g.cm^{-3}$)	Apparent density ($g.cm^{-3}$)	Powder bed apparent density ($g.cm^{-3}$)
A	32	54	95	7.938 ± 0.003	4.9	4.3	4.5
A30	10	16	26	/	5.1	4.2	**4.2**
M	49	71	106	7.926 ± 0.007	4.7	3.7	4
M63	44	59	81	/	4.4	3.6	**3.8**

Table 2: Comparison between several flow indicators for powders A, A30, M and M63.

Powder	Span value	Hausner ratio	Hall flow (s/50g)	Avalanche angle (°)
A	1.18	1.14	18	33
A30	1	1.21	No flow	41
M	0.80	1.27	21	36
M63	0.66	1.22	18	49

Table 3: Oxygen contents of powders A, AM and M63 measured by inert gas fusion

Powder	O content (ppm)
A	1326 ± 7
AM	1295 ± 9
M63	1784 ± 22

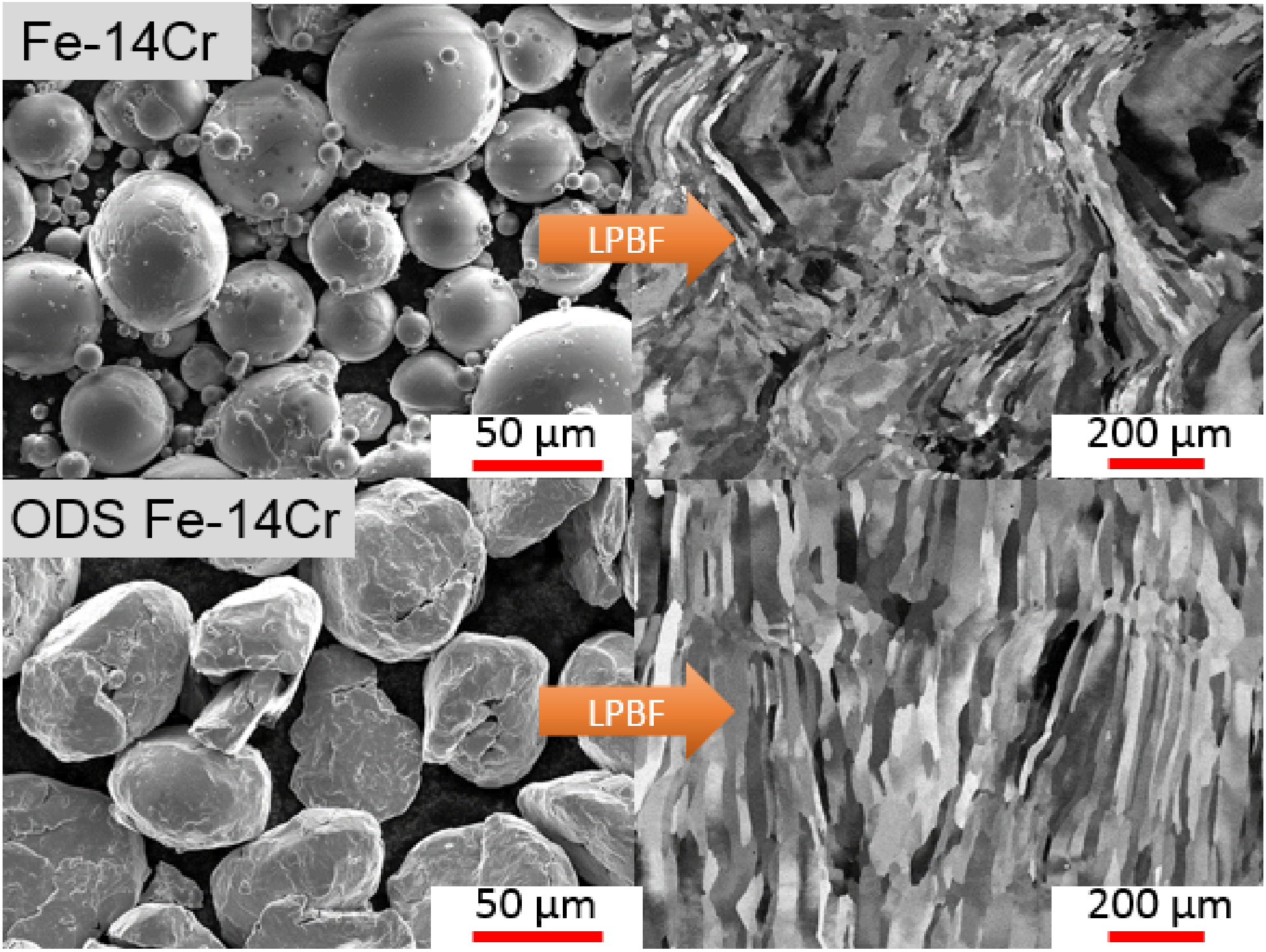
Fe-14Cr
LPBF
50 µm
200 µm
ODS Fe-14Cr
LPBF
50 µm
200 µm